**ADVANCED
SCIENCE NEWS**
www.advancedsciencenews.com

**ADVANCED
MATERIALS**
www.advmat.de

COMMUNICATION

Coordination Polymers Derived General Synthesis of Multishelled Mixed Metal-Oxide Particles for Hybrid Supercapacitors

Bu Yuan Guan, Akihiro Kushima, Le Yu, Sa Li, Ju Li, and Xiong Wen (David) Lou**

Metal–organic frameworks (MOFs) or coordination polymers (CPs) have been used as precursors for synthesis of materials. Unlike crystalline MOF, amorphous CP is nonspecific to metal cation species, therefore its composition can be tuned easily. Here, it is shown that amorphous CP can be used as general synthesis precursors of highly complex mixed metal oxide shells. As a proof of concept, Ni—Co coordination polymer spheres are first synthesized and subsequently transformed into seven-layered Ni—Co oxide onions by rapid thermal oxidation. This approach is very versatile and can be applied to produce ternary and quaternary metal oxide onions with tunable size and composition. The Ni—Co oxide onions exhibit exceptional charge storage capability in aqueous electrolyte with high specific capacitance ($\approx$1900 F g^{-1} at 2 A g^{-1}), good rate capability, and ultrahigh cycling stability (93.6% retention over 20 000 cycles). A hybrid supercapacitor against graphene/ multishelled mesoporous carbon sphere shows a high energy density of 52.6 Wh kg^{-1} at a power density of 1604 W kg^{-1} (based on active materials weight), as well as remarkable cycling stability.

Hollow metal oxide shells with controlled size, composition, and internal structure could be used in a wide range of applications, such as energy storage and conversion, catalysis, and drug delivery.[1–12] Multishell structures can overcome a common drawback of simple hollow shell, namely, the low packing density originating from the large empty space inside. In addition, tunable composition/components may greatly improve the overall performance.[13–15] For example, spinel nickel cobaltite (NiCo$_2$O$_4$) possesses much better electrical conductivity and higher electrochemical activity than Co$_3$O$_4$ or NiO.[16,17] Until now, several types of multishelled metal oxides hollow particles have been successfully synthesized by

templating.[7,18–20] For example, Wang and co-workers synthesized multishelled TiO$_2$ hollow microspheres using carbonaceous microspheres as hard templates, which exhibit higher lithium storage capacity and improved cycling performance compared with single-shelled TiO$_2$ microspheres.[21] Lou et al. have reported a shell-by-shell templating method to fabricate double-shelled SnO$_2$ hollow spheres using silica spheres as hard template.[22] Cu$_2$O hollow spheres with multishelled structures have also been prepared using a cationic surfactant, cetyltrimethylammonium bromide, as soft template.[23] Previously we have reported a new "penetration–solidification–annealing" method to synthesize multishelled mixed metal oxide hollow spheres.[24] Very recently, we have also developed a self-templating strategy to construct uniform NiCo$_2$O$_4$ hollow spheres with a core-double-shell structure.[25] Despite all these advances, the methods developed require tedious multistep synthesis. Also, the number of shells of the hollow particles obtained is generally less than four, limited by the amount of metal cations that can diffuse into the hard templates. Therefore, it is highly desirable to develop a general and efficient method for the synthesis of highly complex multishelled hollow particles with tunable composition.

Coordination polymers (CPs) or more commonly known as metal–organic frameworks (MOFs) are a novel class of materials constructed from metal ions and bridging organic linkers[26–28] and have been proven to be promising precursors.[29–34] For example, Prussian blue analogues Co$_3$[Co(CN)$_6$]$_2$ and Fe$_3$[Fe(CN)$_6$]$_2$ nanocubes have been used to synthesize Co$_3$O$_4$ and Fe$_2$O$_3$ nanoboxes, respectively.[35–37] CuO and CuO/ Cu$_2$O hollow polyhedra have been fabricated by using Cu-based HKUST-1 as the precursors.[38,39] The multicomponent ball-in-ball hybrid metal oxides have also been fabricated by taking advantage of the ion exchange and thermal behavior of coordination polymer spheres (CPSs).[40] Recently, porous spinel Zn$_x$Co$_{3-x}$O$_4$ hollow polyhedra have been reported by utilizing a novel heterobimetallic zeolitic imidazolate frameworks as the precursors.[41] Despite the great progress that has been achieved, it is still challenging to generally derive ternary or quaternary metal oxide hollow structures with highly complex multishelled structures from very limited micro/nanosized

Dr. B. Y. Guan, Dr. L. Yu, Prof. X. W. Lou
School of Chemical and Biomedical Engineering
Nanyang Technological University
62 Nanyang Drive, Singapore 637459, Singapore
E-mail: xwlou@ntu.edu.sg
Dr. A. Kushima, Dr. S. Li, Prof. J. Li
Department of Nuclear Science and Engineering
and Department of Materials Science and Engineering
Massachusetts Institute of Technology
Cambridge, MA 02139, USA
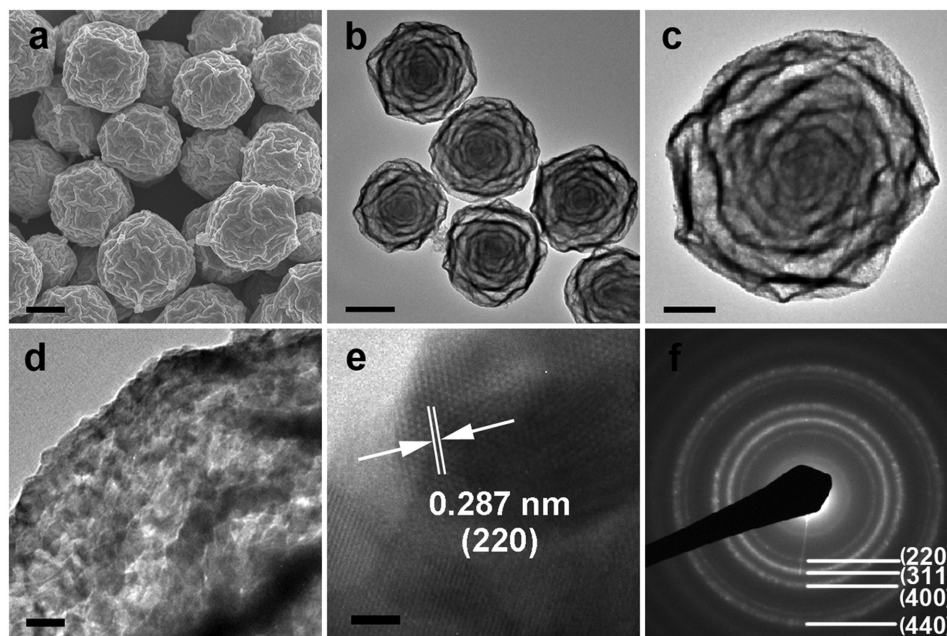E-mail: liju@mit.edu

Figure 1. Microscopy characterizations of multishelled Ni—Co oxide particles. a) FESEM image (scale bar: 500 nm) and b) TEM image (scale bar: 500 nm). Magnified TEM images showing c) an individual multishelled Ni—Co oxide particle (scale bar: 200 nm) and d) the crystalline shell (scale bar: 20 nm). e) High-resolution TEM image of the Ni—Co oxide shell (scale bar: 2 nm) and f) the corresponding SAED pattern.

MOF or CP precursors. One great difficulty lies in the fact that most commonly known MOFs or CPs are crystalline and their formation is highly specific to certain metal cations.

Herein, we synthesize a unique class of amorphous CPSs as the precursor to generate multishelled mixed metal oxides. These amorphous CPSs are nonspecific to the metal cations incorporated, as the carboxylate ligands used have been widely demonstrated to be capable of forming coordinate bonds with most transition metal cations.[42] Therefore, the composition of the derived multishelled particles can be easily controlled. To demonstrate the concept, Ni—Co CPSs are synthesized from coprecipitation of Co^{2+} and Ni^{2+} cations in the presence of organic ligand, isophthalic acid (H_2IPA). These Ni—Co CPSs can be easily oxidized in air, and the oxide layer formed is friable and spalls off on its own, to form seven-layered multishelled Ni—Co oxide particles without any other template. The synthesis approach in this study can be used as a universal route to synthesize multishelled particles of ternary and quaternary metal oxides with tunable size and composition, cheaply and with high yield. We demonstrate the versatility of this approach by synthesizing multishelled particles for many compositions and sizes. With both structural and compositional advantages, multishelled Ni—Co oxide particles manifest remarkable performance as electrode materials for electrochemical capacitors. Finally, liquid-cell in situ transmission electron microscopy observation is performed to investigate the charge/discharge behavior of Ni—Co oxide particles in alkaline electrolyte.

We first synthesize unique Ni—Co CPSs as the precursor from coprecipitation of Co^{2+} and Ni^{2+} cations in the presence of H_2 IPA as the organic ligand via a solvothermal process. Field-emission scanning electron microscopy (FESEM) and transmission electron microscopy (TEM) images show that these Ni—Co CPSs are uniform with an average size of about 1.2 µm (Figure S1, Supporting Information). The powder X-ray diffraction (XRD) indicates the amorphous nature of Ni—Co CPSs (Figure S2, Supporting Information). Fourier transform infrared (FTIR) spectra verify that the band of C=O stretching vibration shifts from 1570 to 1510 cm^{-1} after the formation of CP, demonstrating the coordination of carboxylate groups of H_2IPA to Co^{2+} and Ni^{2+} cations (Figure S3, Supporting Information). After the air thermal oxidation, the Ni—Co CP precursor is converted into Ni—Co oxide. The XRD pattern of the Ni—Co oxide sample is similar to the standard patterns of $NiCo_2O_4$ and Co_3O_4 (Figure S2, Supporting Information), revealing that the mixed Ni—Co oxide also adopts the spinel structure with similar lattice constants. As shown in **Figure 1**a, the as-synthesized Ni—Co oxide particles retain the spherical shape of their CP precursors. However, the diameter of Ni—Co oxide particles is reduced to about 1 µm, which is smaller than that of Ni—Co CPSs due to the shrinkage during calcination. Besides, the surface of the Ni—Co oxide particles becomes crumpled and rough, indicating the formation of thin shells consisting of small oxide nanograins. As revealed by TEM observation in Figure 1b, the as-synthesized Ni—Co oxide particles are composed of highly crumpled layers. Magnified image clearly demonstrates that the multishelled Ni—Co oxide particle possesses a unique seven-layered hollow structure (Figure 1c). Many connection parts between the crumpled neighboring layers can be seen throughout the whole structure, which may improve the structural stability of this material. Polycrystalline texture can be clearly observed within the thin layer of Ni—Co oxide nanoshell (Figure 1d). Consistent with the XRD analysis, a set of distinct lattice fringes with spacing of 0.287 nm can be identified as the (220) planes of Ni—Co spinel oxide (Figure 1e). The distinct

ADVANCED
SCIENCE NEWS
www.advancedsciencenews.com

ADVANCED
MATERIALS
www.advmat.de

COMMUNICATION

selected area electron diffraction (SAED) pattern also confirms the spinel phase of the sample (Figure 1f). Energy-dispersive X-ray spectroscopy (EDX) analysis shows the Ni/Co molar ratio is about 1:1 within the final multishelled Ni−Co oxide particles (Figure S4, Supporting Information), which is in accordance to the relative amount of metal nitrate reactants used for preparation of CP precursors. The chemical composition of the sample is further measured using inductively coupled plasma optical emission spectroscopy (ICP-OES). The Ni/Co molar ratio for the multishelled Ni−Co oxide particles determined by the ICP-OES analysis is about 1:1.09, which is very close to the EDX result. As determined by N_2 sorption, the multishelled Ni−Co oxide particles exhibit a Brunauer–Emmett–Teller (BET) specific surface area of $A = 45$ m^2 g^{-1} (Figure S5, Supporting Information). The mass density of $NiCo_2O_4$ is 5.79 g cm^{-3}, and the mass density of Co_3O_4 is 5.91 g cm^{-3}. Assuming a theoretical density $\rho = 5.7$ g cm^{-3}, a freestanding oxide sheet of thickness $t_{theoretical} = 2/\rho A = 8$ nm would give the same BET specific surface area. It is reasonable to assume that the oxide grain size $D \sim t_{theoretical}$.

The diameter of multishelled Ni−Co oxide particle can be easily tailored in the range of 500 nm–1.6 µm (Figure S6, Supporting Information) by tuning the CPS diameter via simply adjusting the concentration of metal cations and organic ligand in the reaction medium. Notably, the derived multishelled Ni−Co oxide particles are uniform with similar multilayered structures. Even for the smallest particles with a diameter of about 500 nm, six layers of shells can still be recognized. The apparent thickness of each layer is much larger than $t_{theoretical} \sim D$ due to the corrugation and porosity of the shell.

To confirm the versatility of the method, Co_3O_4, NiO, and multishelled Ni−Co oxide particles with controlled Ni/Co molar ratios of 1:2 and 2:1 are synthesized (Figure S7, Supporting Information). FESEM characterizations verify that these four types of multishelled particles exhibit similar features in morphology and uniformity. Moreover, TEM images provide direct evidence that multishelled structures are formed for all these four types of hollow particles with some difference in the number of shells and shell thickness. The molar ratio of Ni and Co elements in each mixed metal oxide material is determined by EDX analysis (Figure S8, Supporting Information).

The carboxylate ligands have been widely demonstrated to be capable of forming coordinate bonds with most transition metal cations and their derived metal carboxylate species can serve as building units toward construction and synthesis of diverse CPs.[42] Of note, we further verify that this strategy can be applied to the synthesis of other multishelled mixed transition-metal oxide (TMO) particles through the thermal oxidation of mixed transition-metal CP precursors. The multishelled particles of mixed TMOs including manganese cobalt oxide (Mn−Co oxide), manganese nickel oxide (Mn−Ni oxide), zinc manganese oxide (Zn−Mn oxide), and manganese cobalt nickel oxide (Mn−Co−Ni oxide) are obtained. **Figure 2** shows the morphology and interior architecture of these four types of multishelled mixed metal oxide particles. FESEM images confirm that these four types of multishelled particles own similar features in crumpled morphology and size uniformity. Moreover, TEM characterizations provide further evidence that multishelled structures are formed for these four types of hollow particles. The crystal structure and chemical composition of each mixed metal oxide material are verified by XRD (Figure S9, Supporting Information) and EDX (Figure S10, Supporting Information), respectively.

The formation of these multishelled metal oxide particles through the thermal decomposition of CP precursors is mainly based on the heterogeneous contraction caused by heat treatment.[43] **Figure 3**a schematically illustrates the morphological and structural evolution of the multishelled metal oxide particle from the solid CPS. We take the Ni−Co oxide sample as an example. TEM is used to characterize the intermediates collected at different thermal decomposition stages. The structural change from solid CPS to multishelled mixed metal oxide particle involves several stages (Figure 3b–e). It has to do with the so-called "friable oxide" or oxide spallation phenomena in oxidation, where the large volume change (in this case shrinkage due to the large weight loss of ≈75%, Figure S11, Supporting Information) from CP to oxide induces residual stress in the oxide layer, and causes spallation once the oxide layer reaches
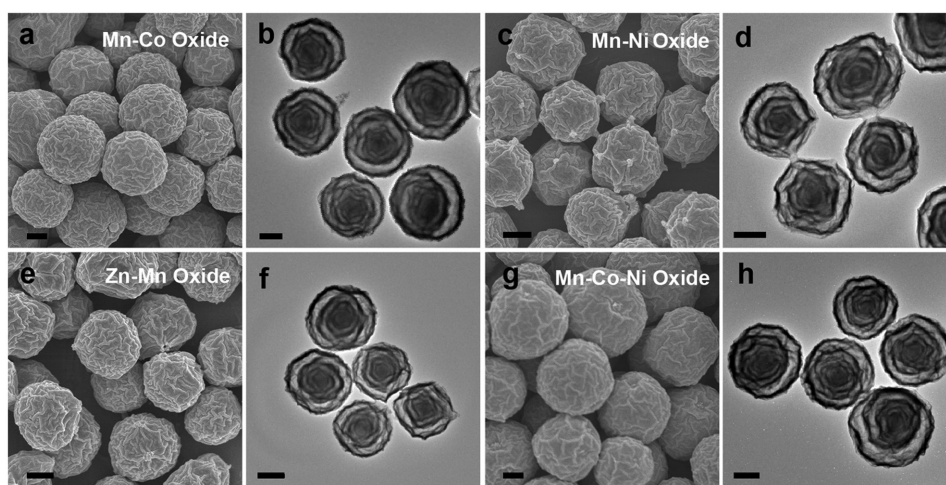

Figure 2. FESEM and TEM images of ternary and quaternary metal oxide multishelled particles. a,b) Mn−Co oxide, c,d) Mn−Ni oxide, e,f) Zn−Mn oxide, and g,h) Mn−Co−Ni oxide multishelled particles. All scale bars are 500 nm.
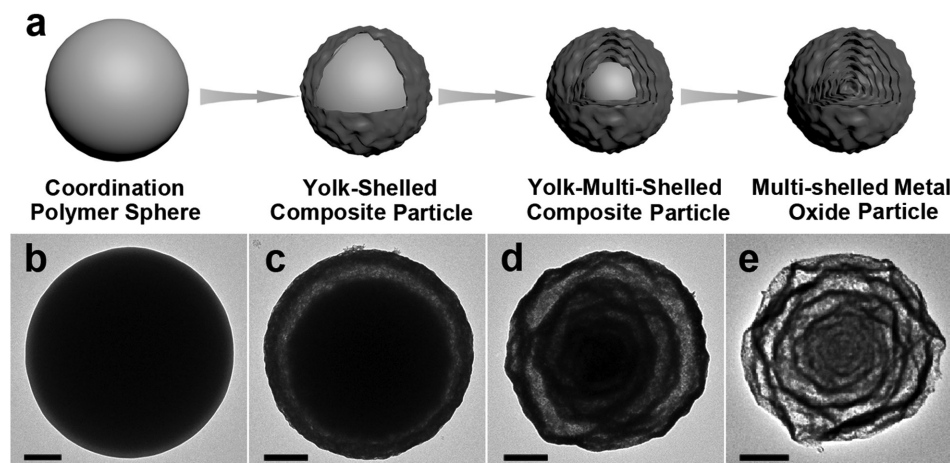
Figure 3. The formation process of the multishelled structure. a) Schematic illustration of the formation process. TEM images of b) Ni—Co CPS and the products obtained after calcination of CPS to different temperatures: c) 360 °C, d) 390 °C, e) 500 °C. The scale bars in (b–e) are 200 nm.

a critical thickness, to form a yolk-shelled structure when the temperature reaches about 360 °C (Figure 3c). Due to residual stress of the phase transformation and adhesion force, the oxide layer has a crumpled morphology. With prolonged heating, the same contraction process continues to take place. A yolk-multi-shelled structure is formed when the temperature is increased to about 390 °C (Figure 3d). By further increasing the temperature to 500 °C, the seven-layered particle is formed (Figure 3e). It is well known that friable oxides tend to have a lot of cracks

within (as they are nonprotective against further oxidation for the metal beneath despite μm thickness, in contrast to the protective SiO_2, Al_2O_3, Cr_2O_3 oxide layers that are just sub-10 nm in thickness), so we expect the shells to be partly porous.

We have evaluated the electrochemical properties of the multishelled Ni—Co oxide particles with the Ni/Co molar ratio of 1:1 by using a three-electrode cell in 6.0 M KOH solution. The cyclic voltammetry (CV) curves of the Ni—Co oxide electrode with different sweep rates are shown in **Figure 4**a. A pair of
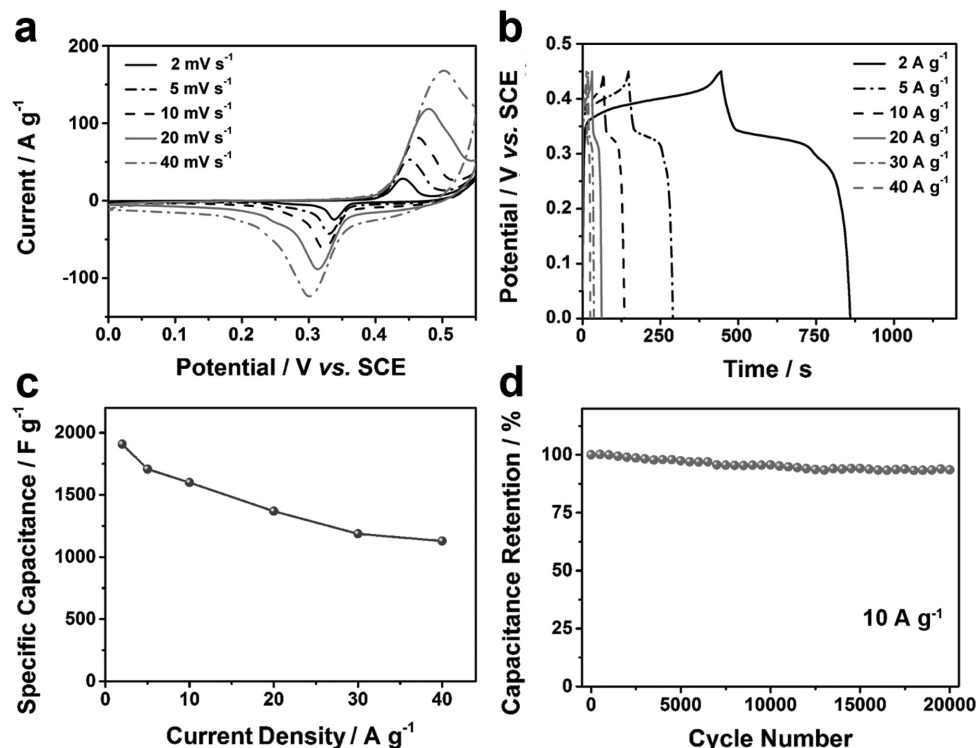

Figure 4. Electrochemical characterizations of the multishelled Ni—Co oxide particles. a) CV curves at different sweep rates. b) Galvanostatic charge–discharge curves at various current densities, and c) the corresponding specific capacitance calculated from the discharge curves. d) The cycling performance at a constant current density of 10 A g^{-1}.

redox peaks can be observed within the potential range from 0 to 0.55 V versus saturated calomel electrode (SCE) at all sweep rates, indicating the presence of Faradaic redox reactions related to M—O/M—O—OH (M represents Ni or Co).[44,45] Further, from the plots of peak current density (I_p) versus square root of sweep rate ($v^{1/2}$) from 2 to 40 mV s^{-1} for both cathodic and anodic peaks (Figure S12, Supporting Information), the current obeys a power-law relationship with the sweep rate ($I_p = av^b$). Whereas a b-value of 0.5 indicates that the current is controlled by semi-infinite linear diffusion, a value of 1.0 indicates that the current is surface-controlled. For sweep rates ranging from 2 to 40 mV s^{-1}, a linear relationship is observed between I_p and $v^{1/2}$ for both cathodic and anodic peaks, indicating that the kinetic is a diffusion-controlled process. Figure 4b presents the galvanostatic charge–discharge curves of the Ni—Co oxide electrode at different current densities ranging from 1 to 40 A g^{-1}. In principle, this class of materials gives battery-type conversion electrodes, at least when the grain size D is large. With shrinking D, however, it can gradually transition to pseudocapacitive-type behavior due to rapid surface/interfacial diffusions and facile transformations in the near-interface material.[46] For the sake of easy comparison to numerous other works in literature, we report here the charge storage capacity in terms of specific capacitance. The calculated specific capacitance as a function of the discharge current density is shown in Figure 4c. A maximum specific capacitance reaches up to 1908 F g^{-1} measured at a discharge current density of 2 A g^{-1}, in a voltage scanning window of $\Delta U = 0.45$ V. With the increase of current density, the capacitance of the Ni—Co oxide electrode gradually decreases. The Ni—Co oxide electrode still delivers relatively high specific capacitance of 1707, 1600, 1369, 1187, and 1129 F g^{-1} at current densities of 5, 10, 20, 30, and 40 A g^{-1}, respectively. About 71.7% of the capacitance for multishelled Ni—Co oxide particles is retained when the current density increases from 2 to 20 A g^{-1}. The cycling performance of the Ni—Co oxide electrode is evaluated by the continuous charging–discharging test at a current density of 10 A g^{-1} (Figure 4d). Impressively, the multishelled Ni—Co oxide particles manifest exceptional cycling stability and deliver 93.6% of its initial capacitance even after 20 000 cycles. After cycling, the multishelled structure can be well retained (Figure S13, Supporting Information). The multishelled Ni—Co oxide particles with the Ni/Co molar ratio of 1:2 also exhibit similar rate capability and cycling performance (Figure S14, Supporting Information). The electrochemical performance of multishelled Ni—Co particles is superior to that of many Ni—Co based metal oxides and other mixed metal oxide materials (Table S1, Supporting Information), which must be related to advantageous structural features of the multishelled Ni—Co oxide particles, to be discussed next.

To further evaluate the Ni—Co oxide electrode for practical applications, a hybrid supercapacitor (HSC) device is fabricated using the Ni—Co oxide electrode as the cathode and graphene/multishelled mesoporous carbon sphere (G/MMCS) composite electrode (Figure S15, Supporting Information) as the anode in 6.0 M KOH solution (**Figure 5**a). The typical CV curves of the Ni—Co oxide//G/MMCS HSC device at various sweep rates between 0 and 1.6 V are shown in Figure 5b. A combination of both pseudocapacitive and electric double-layer types of capacitance can be seen at all sweep rates. Figure 5c reveals the galvanostatic charge–discharge profiles at different current densities. The discharge curves are almost symmetrical to the corresponding charge curves, suggesting excellent charge-storage reversibility of the HSC device. Figure 5d shows the specific capacitance calculated from the discharge curves. The Ni–Co oxide//G/MMCS HSC device achieves a relatively high specific capacitance of 149 F g^{-1} (based on active materials weight) at a current density of 2.0 A g^{-1}. Moreover, the HSC device exhibits excellent rate capability with 82.5% of capacitance retained even at the current density of 20 A g^{-1}. The cycling performance of the HSC device at a current density of 10 A g^{-1} is shown in Figure 5e. Remarkably, the HSC device manifests very high cycling stability and is able to deliver 91.3% of its initial capacitance even after 10 000 cycles. The Ragone plots of Ni—Co oxide//G/MMCS HSC device derived from the discharge curves are shown in Figure 5f. Impressively, a high energy density of 52.6 Wh kg^{-1} can be obtained at a power density of 1604 W kg^{-1} and the energy density still retains 29.6 Wh kg^{-1} even at higher power density of 28 800 W kg^{-1}, which show enhanced electrochemical performance compared with many previously reported hybrid systems (Table S2, Supporting Information), such as Ni$_x$Co$_{1-x}$ oxide//AC,[47] Co$_3$O$_4$//AC,[48] Ni(OH)$_2$-CNT//AC,[49] and NiCo$_2$S$_4$//G/CS.[8]

Strain accommodation is a well-recognized essential problem in battery-type conversion electrodes.[50] It is extremely intriguing to consider how the transformation strains are accommodated very rapidly for tens of thousands of cycles in pseudocapacitor electrodes, in a supposedly brittle ceramics. Figure 4b shows that 2 A g^{-1} × 420 s = 230 mAh g^{-1} of charge can be reversibly taken in and out of the electrode very quickly, for 20 000 cycles. This large amount (comparable to advanced battery cathode materials) cannot be just surface charge storage, and insertion of ions and interior redox of Ni, Co cations in the grains (could be in near-surface or near-grain boundary regions, considering $D \sim t_{theoretical} = 8$ nm) must be involved. Previously, with electrochemical quartz crystal microbalance, it was determined that insertion/extraction of multiple water molecules often accompany one redox reaction in aqueous pseudocapacitor materials.[51] Assuming a volume change of just 0.5 water molecule (≈ 15 Å^3) per redox electron transfer, this would still require a volume expansion $\Delta V/V \approx 30\%$ of the hydrated metal oxide. How can fragile-looking structures like Figure 1c,d accommodate the huge expansion and shrinkage of Ni—Co oxide grains is the mystery we want to reveal with in situ liquid-cell TEM.

We next conduct in situ TEM observation to understand the charge/discharge process of multishelled Ni—Co oxide particles. A liquid confining cell[52] is used to encapsulate the aqueous electrolyte preventing it from evaporating in the high vacuum inside TEM. The multishelled Ni—Co oxide particles are used as the cathode and W metal as the anode in 6.0 M KOH solution. A constant voltage charge/discharge is performed by repeating 20 s of charge biased at 1.0 V on the Ni—Co oxide versus W electrode and 20 s of discharge at −0.3 V. **Figure 6**a shows the change in the Ni—Co oxide particle during the charge/discharge process (see also Movie S1, Supporting Information). Only small apparent volume expansion and contraction of the shell are observed during the cycling. The outer shell
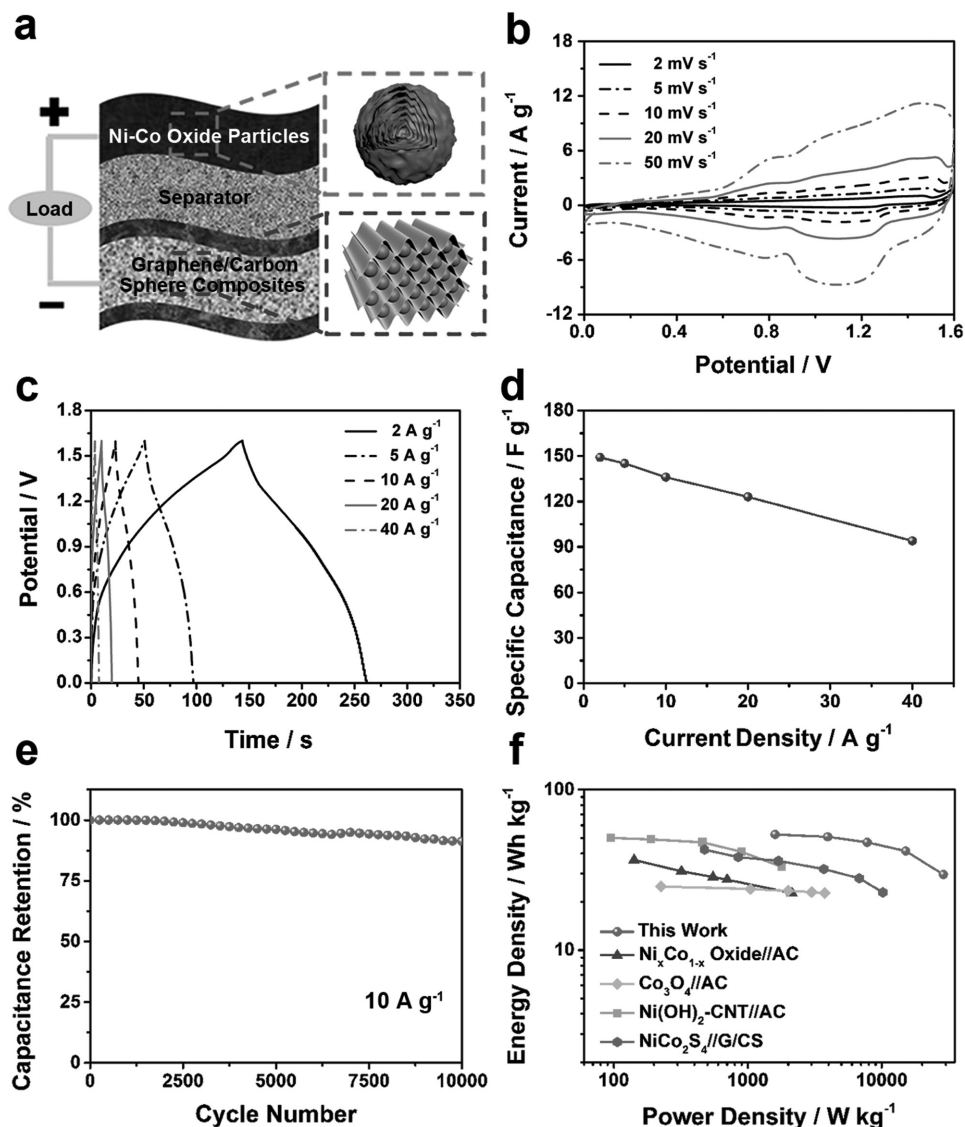
COMMUNICATION

Figure 5. Electrochemical evaluation of the Ni—Co oxide//G/MMCS HSC device. a) Schematic illustration of the HSC device. b) CV curves at different sweep rates. c) Galvanostatic charge/discharge voltage profiles at various current densities, and d) the corresponding specific capacitance calculated from the discharge curves. e) The cycling performance and f) Ragone plot of the HSC device.

bulges a bit upon charge, which shrinks back at discharge, as indicated by the arrowheads in the figure. Figure 6b shows the change in the Ni—Co oxide particle diameter/during the cyclic charge/discharge. The change is within a few percent, but slight increase in the particle diameter is observed as the cycle number is increased. This change may be associated with the change in the wrinkle pattern of the shell. It is also highly likely that the shells are porous, so the void spaces in the grain aggregation can accommodate the substantial volume change of individual grains due to Faradaic redox reactions, related to M—O/M—O—OH (M represents Ni or Co) and water insertion/extraction.[44,45] Such well-accommodated volume changes at nanograin level are seen to drive only minimum overall structural alteration of the multishelled particles, during rapid charging/discharging, contributing to the extremely high cyclability of the electrode.

To explore the structural stability limit of the multishelled particles, we applied a higher voltage (still before electrolyte decomposition and gas evolution, which we have seen at higher and lower voltages, see Movie S2 (Supporting Information) at 2.0 V and Movie S3 (Supporting Information) at −0.7 V). Figure 6c shows the change in the multishelled Ni—Co oxide particle charged at 1.4 V (see also Movie S4, Supporting Information). The shells disintegrate to smaller particles and scatter into the electrolyte. The highly concentrated OH⁻ ions on the nanoparticles may cause repulsion between them and eventually destroy the shell structure as schematically illustrated in Figure 6d. Multiple factors such as applied voltage, current density, and the structure of the multishelled particles (nanoparticle size, packing density, etc.) need to be considered to understand the criteria to initiate this failure, which is not the focus of the present work. The explosion of the particle shown
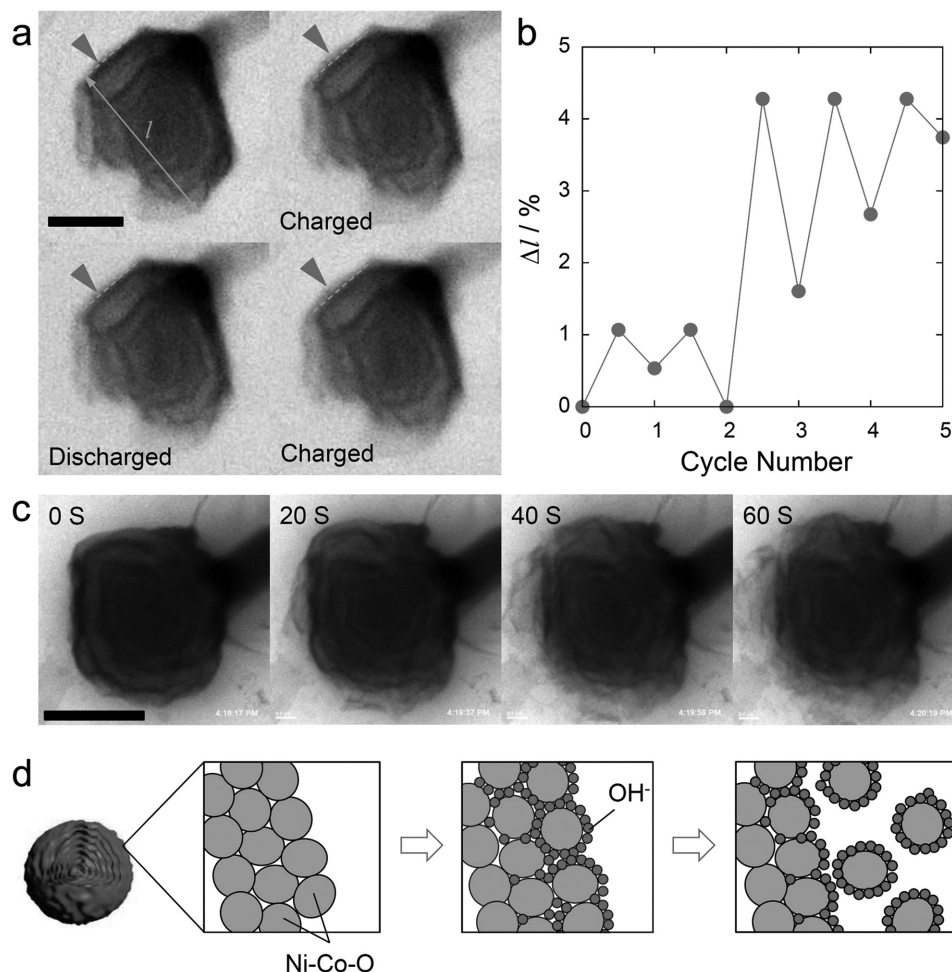
Figure 6. In situ liquid-cell TEM observation of charge/discharge process. a) Change in the multishelled Ni–Co oxide particle shape in the charge/discharge process. The arrow heads indicate the bulging of the outer shell. The dashed line is the guide for the eyes. See also Movie S1, Supporting Information. b) The particle size evolution in the repeating charge/discharge cycles. c) Fracturing of the particle during charge. See also Movie S4, Supporting Information. d) Schematic illustration explaining the nanoparticle dissociation from the shell. The scale bars in (a) and (c) are 1 μm.

here may be the extreme case. But detachment of individual nanoparticles from the shell at lower voltages can still be one of the factors causing the irreversible capacity loss. The scattered nanograins are very small, with sub-10 nm grain size D. Such extremely small grain sizes and porous shell would support prolific and percolating surface/interfacial diffusion pathways and facile transformations in the near-interface material[53] and pseudocapacitive-type behavior.[46] The excellent strain accommodation at the shell level and structural integrity of the multishelled particle despite the necessarily large volume expansion of the nanograins, revealed by in situ TEM before the disintegration voltage, gives a microscopic explanation for the excellent cyclability (10^4 cycles, much better than typical battery-type electrodes) of our electrode, that apparently possesses similar charge storage ability as advanced battery cathode materials ($\approx$230 mAh g^{-1}).

In summary, a general method is developed to prepare highly complex multishelled mixed metal-oxide particles. The key feature of the new method is that a novel class of amorphous coordination polymers serves as the precursors for the effective formation of various multishelled mixed metal-oxide particles by a subsequent thermal treatment. This provides the platform for making many designed multishelled metal oxide particles with tailored size, number of shell layers, and composition. As a demonstration, the multishelled Ni–Co oxide particles exhibit exceptional charge storage capability in aqueous electrolyte with high specific capacitance ($\approx$1900 F g^{-1} at 2 A g^{-1}), good rate capability, and ultrahigh cycling stability (93.6% retention over 20 000 cycles). A hybrid supercapacitor against graphene/multishelled mesoporous carbon sphere shows a high energy density of 52.6 Wh kg^{-1} at a power density of 1604 W kg^{-1} (based on active materials weight), as well as remarkable cycling stability. As demonstrated by the liquid-cell in situ transmission electron microscopy observation, the volume change of the oxide nanograins is well-accommodated at the shell level during the charge/discharge process in alkaline electrolyte, which is believed to be the reason for the remarkable electrochemical performance and longevity. The present recipe offers a new way to precisely control the structure and composition of multishelled metal oxide particles for a wide range of applications.

COMMUNICATION

Supporting Information

Supporting Information is available from the Wiley Online Library or from the author.

[1] M. H. Oh, T. Yu, S.-H. Yu, B. Lim, K.-T. Ko, M.-G. Willinger, D.-H. Seo, B. H. Kim, M. G. Cho, J.-H. Park, K. Kang, Y.-E. Sung, N. Pinna, T. Hyeon, *Science* **2013**, *340*, 964.

[2] A. J. Brown, N. A. Brunelli, K. Eum, F. Rashidi, J. R. Johnson, W. J. Koros, C. W. Jones, S. Nair, *Science* **2014**, *345*, 72.

[3] Z. Wang, L. Zhou, X. W. Lou, *Adv. Mater.* **2012**, *24*, 1903.

[4] D. S. Bykov, O. A. Schmidt, T. G. Euser, P. S. J. Russell, *Nat. Photonics* **2015**, *9*, 461.

[5] A. Carné-Sánchez, I. Imaz, M. Cano-Sarabia, D. Maspoch, *Nat. Chem.* **2013**, *5*, 203.

[6] B. Y. Xia, Y. Yan, N. Li, H. B. Wu, X. W. Lou, X. Wang, *Nat. Energy* **2016**, *1*, 15006.

[7] J. Wang, H. Tang, L. Zhang, H. Ren, R. Yu, Q. Jin, J. Qi, D. Mao, M. Yang, Y. Wang, P. Liu, Y. Zhang, Y. Wen, L. Gu, G. Ma, Z. Su, Z. Tang, H. Zhao, D. Wang, *Nat. Energy* **2016**, *1*, 16050.

[8] L. Shen, L. Yu, H. B. Wu, X.-Y. Yu, X. Zhang, X. W. Lou, *Nat. Commun.* **2015**, *6*, 6694.

[9] B. Y. Guan, L. Yu, J. Li, X. W. Lou, *Sci. Adv.* **2016**, *2*, e1501554.

[10] Y. M. Chen, X. Y. Yu, Z. Li, U. Paik, X. W. Lou, *Sci. Adv.* **2016**, *2*, e1600021.

[11] B. Y. Guan, L. Yu, X. W. Lou, *Adv. Mater.* **2016**, DOI: 10.1002/adma.201605051.

[12] Y. Boyjoo, M. Wang, V. K. Pareek, J. Liu, M. Jaroniec, *Chem. Soc. Rev.* **2016**, *45*, 6013.

[13] J. Liu, S. Z. Qiao, S. Budi Hartono, G. Q. Lu, *Angew. Chem., Int. Ed.* **2010**, *49*, 4981.

[14] X. Lai, J. E. Halpert, D. Wang, *Energy Environ. Sci.* **2012**, *5*, 5604.

[15] H. Liu, J. B. Joo, M. Dahl, L. Fu, Z. Zeng, Y. Yin, *Energy Environ. Sci.* **2015**, *8*, 286.

[16] L. Huang, D. Chen, Y. Ding, S. Feng, Z. L. Wang, M. Liu, *Nano Lett.* **2013**, *13*, 3135.

[17] T.-Y. Wei, C.-H. Chen, H.-C. Chien, S.-Y. Lu, C.-C. Hu, *Adv. Mater.* **2010**, *22*, 347.

[18] Z. Dong, H. Ren, C. M. Hessel, J. Wang, R. Yu, Q. Jin, M. Yang, Z. Hu, Y. Chen, Z. Tang, H. Zhao, D. Wang, *Adv. Mater.* **2014**, *26*, 905.

[19] S. Peng, L. Li, Y. Hu, M. Srinivasan, F. Cheng, J. Chen, S. Ramakrishna, *ACS Nano* **2015**, *9*, 1945.

[20] J. Wang, N. Yang, H. Tang, Z. Dong, Q. Jin, M. Yang, D. Kisailus, H. Zhao, Z. Tang, D. Wang, *Angew. Chem., Int. Ed.* **2013**, *52*, 6417.

[21] H. Ren, R. Yu, J. Wang, Q. Jin, M. Yang, D. Mao, D. Kisailus, H. Zhao, D. Wang, *Nano Lett.* **2014**, *14*, 6679.

[22] X. W. Lou, C. Yuan, L. A. Archer, *Small* **2007**, *3*, 261.

[23] H. Xu, W. Wang, *Angew. Chem., Int. Ed.* **2007**, *46*, 1489.

[24] G. Zhang, X. W. Lou, *Angew. Chem., Int. Ed.* **2014**, *53*, 9041.

[25] L. Shen, L. Yu, X.-Y. Yu, X. Zhang, X. W. Lou, *Angew. Chem., Int. Ed.* **2015**, *54*, 1868.

[26] H.-C. Zhou, J. R. Long, O. M. Yaghi, *Chem. Rev.* **2012**, *112*, 673.

[27] Z. Zhang, Y. Chen, S. He, J. Zhang, X. Xu, Y. Yang, F. Nosheen, F. Saleem, W. He, X. Wang, *Angew. Chem., Int. Ed.* **2014**, *53*, 12517.

[28] Y. Li, J. Tang, L. He, Y. Liu, Y. Liu, C. Chen, Z. Tang, *Adv. Mater.* **2015**, *27*, 4075.

[29] O. N. Risset, E. S. Knowles, S. Ma, M. W. Meisel, D. R. Talham, *Chem. Mater.* **2013**, *25*, 42.

[30] H.-L. Jiang, Q. Xu, *Chem. Commun.* **2011**, *47*, 3351.

[31] R. Wu, X. Qian, X. Rui, H. Liu, B. Yadian, K. Zhou, J. Wei, Q. Yan, X.-Q. Feng, Y. Long, L. Wang, Y. Huang, *Small* **2014**, *10*, 1932.

[32] J.-U. Park, H. J. Lee, W. Cho, C. Jo, M. Oh, *Adv. Mater.* **2011**, *23*, 3161.

[33] W. Guo, W. Sun, Y. Wang, *ACS Nano* **2015**, *9*, 11462.

[34] B. Y. Guan, L. Yu, X. W. Lou, *Energy Environ. Sci.* **2016**, *9*, 3092.

[35] L. Zhang, H. B. Wu, S. Madhavi, H. H. Hng, X. W. Lou, *J. Am. Chem. Soc.* **2012**, *134*, 17388.

[36] N. Yan, L. Hu, Y. Li, Y. Wang, H. Zhong, X. Hu, X. Kong, Q. Chen, *J. Phys. Chem. C* **2012**, *116*, 7227.

[37] M. Hu, A. A. Belik, M. Imura, K. Mibu, Y. Tsujimoto, Y. Yamauchi, *Chem. Mater.* **2012**, *24*, 2698.

[38] R. Wu, X. Qian, F. Yu, H. Liu, K. Zhou, J. Wei, Y. Huang, *J. Mater. Chem. A* **2013**, *1*, 11126.

[39] L. Li, S. Peng, Y. Cheah, P. Teh, J. Wang, G. Wee, Y. Ko, C. Wong, M. Srinivasan, *Chem. Eur. J.* **2013**, *19*, 5892.

[40] W. Cho, Y. H. Lee, H. J. Lee, M. Oh, *Adv. Mater.* **2011**, *23*, 1720.

[41] R. Wu, X. Qian, K. Zhou, J. Wei, J. Lou, P. M. Ajayan, *ACS Nano* **2014**, *8*, 6297.

[42] D. J. Tranchemontagne, J. L. Mendoza-Cortes, M. O'Keeffe, O. M. Yaghi, *Chem. Soc. Rev.* **2009**, *38*, 1257.

[43] J. Guan, F. Mou, Z. Sun, W. Shi, *Chem. Commun.* **2010**, *46*, 6605.

[44] P. Simon, Y. Gogotsi, B. Dunn, *Science* **2014**, *343*, 1210.

[45] Q. Zhou, X. Wang, Y. Liu, Y. He, Y. Gao, J. Liu, *J. Electrochem. Soc.* **2014**, *161*, A1922.

[46] K. He, H. L. Xin, K. Zhao, X. Yu, D. Nordlund, T.-C. Weng, J. Li, Y. Jiang, C. A. Cadigan, R. M. Richards, M. M. Doeff, X.-Q. Yang, E. A. Stach, J. Li, F. Lin, D. Su, *Nano Lett.* **2015**, *15*, 1437.

[47] Y.-M. Wang, X. Zhang, C.-Y. Guo, Y.-Q. Zhao, C.-L. Xu, H.-L. Li, *J. Mater. Chem. A* **2013**, *1*, 13290.

[48] C. Zhang, L. Xie, W. Song, J. Wang, G. Sun, K. Li, *J. Electroanal. Chem.* **2013**, *706*, 1.

[49] Z. Tang, C.-h. Tang, H. Gong, *Adv. Funct. Mater.* **2012**, *22*, 1272.

[50] X. H. Liu, Y. Liu, A. Kushima, S. L. Zhang, T. Zhu, J. Li, J. Y. Huang, *Adv. Energy Mater.* **2012**, *2*, 722.

[51] C. A. Beasley, M. B. Sassin, J. W. Long, *J. Electrochem. Soc.* **2015**, *162*, A5060.

[52] A. Kushima, T. Koido, Y. Fujiwara, N. Kuriyama, N. Kusumi, J. Li, *Nano Lett.* **2015**, *15*, 8260.

[53] B. Kang, G. Ceder, *Nature* **2009**, *458*, 190.

ADVANCED MATERIALS

Supporting Information

Coordination Polymers Derived General Synthesis of Multishelled Mixed Metal-Oxide Particles for Hybrid Supercapacitors

Bu Yuan Guan, Akihiro Kushima, Le Yu, Sa Li, Ju Li,* and Xiong Wen (David) Lou*

Supporting Information

Coordination Polymers Derived General Synthesis of Multi-Shelled Mixed Metal-Oxide Particles for Hybrid Supercapacitors

Bu Yuan Guan, Akihiro Kushima, Le Yu, Sa Li, Ju Li,* and Xiong Wen (David) Lou*

[*] Dr. B. Y. Guan, Dr. L. Yu, Prof. X. W. Lou

School of Chemical and Biomedical Engineering, Nanyang Technological University, 62 Nanyang Drive, Singapore, 637459, (Singapore)

Email: xwlou@ntu.edu.sg;　Webpage: http://www.ntu.edu.sg/home/xwlou/

Dr. A. Kushima, Dr. S. Li, Prof. J. Li

Department of Nuclear Science and Engineering and Department of Materials Science and Engineering, Massachusetts Institute of Technology, Cambridge, MA 02139, USA

Email: liju@mit.edu

Experimental details

Synthesis of multi-shelled Ni-Co oxide particles with different sizes. All chemicals and solvents were purchased from commercial sources and used without purification. Take the synthesis of multi-shelled Ni-Co oxide particles with the diameter of about 1 μm as an example, 0.04 mmol of $Co(NO_3)_2$ $6H_2O$, 0.04 mmol of $Ni(NO_3)_2$ $6H_2O$, and 0.08 mmol of isophthalic acid (H_2IPA) were dissolved in a mixture of DMF (5 mL) and acetone (5 mL) to form a clear solution by stirring for 6 h. The solution was then transferred to a Teflon-lined stainless steel autoclave and kept at 160 ^{o}C for 4 h. After cooling to room temperature, the obtained Ni-Co coordination polymer spheres (CPSs) were separated by centrifugation. The multi-shelled Ni-Co oxide particles with the diameter of about 1 μm were generated through a thermal treatment of Ni-Co CPSs in air at the temperature of 500 ^{o}C for 10 min with a heating rate of 5 ^{o}C min^{-1}. To synthesize multi-shelled Ni-Co oxide particles with the particle size of 1.6 μm, 800 nm, or 500 nm, 133%, 67%, or 33% of initial dosage of metal nitrates and organic ligand was used in the synthesis of the coordination polymer (CP) precursors. The multi-shelled particles were obtained via a thermal treatment of the corresponding CP precursors.

Synthesis of multi-shelled Co_3O_4, NiO, and Ni-Co oxide particles with different molar ratios of Ni and Co elements. The synthesis procedures of multi-shelled Co_3O_4, NiO, and Ni-Co oxide particles with Ni/Co molar ratios of 1:2 and 2:1 are similar to those of multi-shelled Ni-Co oxide particles with Ni/Co molar ratio of 1:1 except for using cobalt nitrate, nickel nitrate or the mixture of them with the molar ratios of 1:2 and 2:1 as reactants to prepare the CP precursors. The multi-shelled particles were generated through a thermal treatment of the corresponding CP precursors.

Synthesis of other multi-shelled mixed metal oxide particles. The synthesis procedures of other multi-shelled mixed metal oxide particles are similar to those of multi-shelled Ni-Co oxide particles except for using the mixture of different metal nitrates as reactants to prepare the CP precursors. The multi-shelled particles were obtained via a thermal treatment of the corresponding CP precursors.

Synthesis of graphene/multi-shelled mesoporous carbon sphere composites. Multi-shelled mesoporous carbon spheres (MMCSs) were prepared by a modified method reported by Liu *et al.*.[1] The graphene/multi-shelled mesoporous carbon sphere (G/MMCS) composites were prepared according to the method reported by our group.[2]

Materials characterization. The crystal phase of the products was examined by X-ray diffraction (XRD) on a Bruker D2 Phaser X-Ray Diffractometer. Field-emission scanning electron microscope (FESEM; JEOL-6700F) and transmission electron microscope (TEM; JEOL, JEM-2010) were used to examine the morphology of the samples. The composition of the samples was analyzed by energy-dispersive X-ray spectroscope (EDX) attached to the FESEM instrument. The nitrogen sorption measurement was carried on Autosorb 6B at liquid-nitrogen temperature. Thermogravimetric analysis (TGA) was performed on SDT Q600 (TA Instruments). Fourier transform infrared spectroscopy (FTIR, Imaging Golden Gate, Specac, UK) was conducted in the range of 2000-400 cm^{-1} .

Electrochemical measurements. The working electrode consists of 70 wt% of active material, 20 wt% of conductive carbon black (Super-P-Li), and 10 wt% of polymer binder (polyvinylidene fluoride, PVDF). The mixture was then pressed onto a Ni foam as the working electrode and dried at 120 ^{o}C for 12 h under vacuum. Electrochemical measurements were conducted with a CHI 660D electrochemical workstation in an aqueous KOH electrolyte (6.0 M) using a three-electrode cell, where a Pt foil serves as the counter electrode and a saturated calomel electrode (SCE) as the reference electrode. The specific capacitance of the electrodes was calculated from the chronopotentiometry curves based on the following equation: $C = I\Delta t/m\Delta V$, where I is the discharge current, Δt is the discharge time, ΔV is the voltage range, and m is the mass of the electroactive materials.

Fabrication and evaluation of hybrid supercapacitors. Hybrid supercapacitors (HSCs) were fabricated by assembling Ni-Co oxide cathode and G/MMCS anode in two electrode simulation cells. A 6.0 M KOH solution was employed as the electrolyte. The mass ratio of positive electrode to negative electrode was decided according to the well-known charge balance equation ($q_+= q_-$). In the relation, the charge stored by each electrode usually depends on the specific capacitance (C), the potential range (ΔV) and the mass of the electrode (m) following equation: $q = mC\Delta V$. To obtain $q_+= q_-$, the mass balance will be expressed as following equation: $m_+/m_- = C_-\Delta V_-/C_+\Delta V_+$, C_+ and C_- are the specific capacitance of the Ni-Co oxide and G/MMCS electrodes, respectively. ΔV_+ and ΔV_- are the voltage range of one scanning segment of Ni-Co oxide and G/MMCS electrodes, respectively. The loading mass of multi-shelled Ni-Co oxide particles and graphene/multi-shelled carbon spheres on nickel foams are about 0.32 and 1.52 mg cm^{-2}, respectively. The specific

capacitance (C) of the hybrid supercapacitor is calculated from the chronopotentiometry curves according to the following equation: $C = I\Delta t/m\Delta V$, where I is the discharge current, Δt is the discharge time, ΔV is the voltage range, and m is the total mass of active materials on both electrodes. The energy density (E) and power density (P) of ASC against the two electrodes in device were calculated based on the total mass of the active materials using the following equations: $E = 1/2CV^2$ and $P = E/\Delta t$, where V is the potential change during the discharge process and Δt is the discharge time.

In-situ liquid-cell TEM observation. In-situ TEM observation of the Ni-Co oxide electrode was conducted using the liquid confining cell.[3] The cell consists of two chips with electron-beam-transparent silicon nitride membrane windows. One of the chips has gold electrode patterned on the window as a current collector and the other chip has large W pad deposited on the chip outside the viewing area. The Ni-Co oxide multi-shelled particles were dispersed on the gold electrode and Pt was deposited using FEI Nanolab™ Helios 600 DualBeam FIB/SEM to connect the particles with the gold current collector. After the chip was assembled, a 6.0 M KOH solution was injected as the electrolyte and sealed with epoxy glue. The chip was then mounted on Nanofactory scanning tunneling microscopy (STM)-TEM holder for the observation. JEOL 2010F transmission electron microscope was used for the imaging and Gamry Reference 3000 was used for biasing.
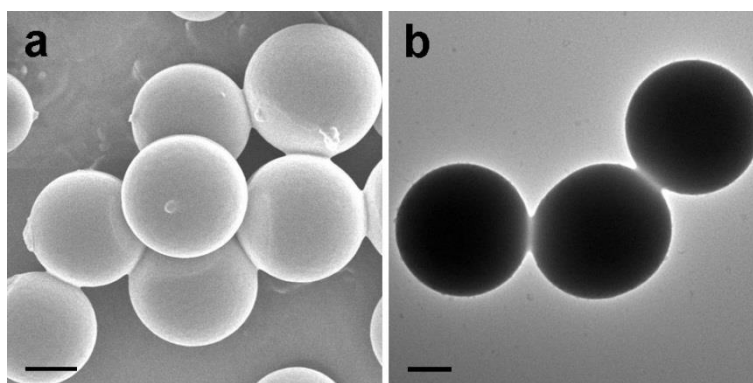
Figure S1. Microscopy characterizations of Ni-Co coordination polymer spheres (CPSs). (a) FESEM and (b) TEM images of Ni-Co CPSs. The scale bars are 500 nm.
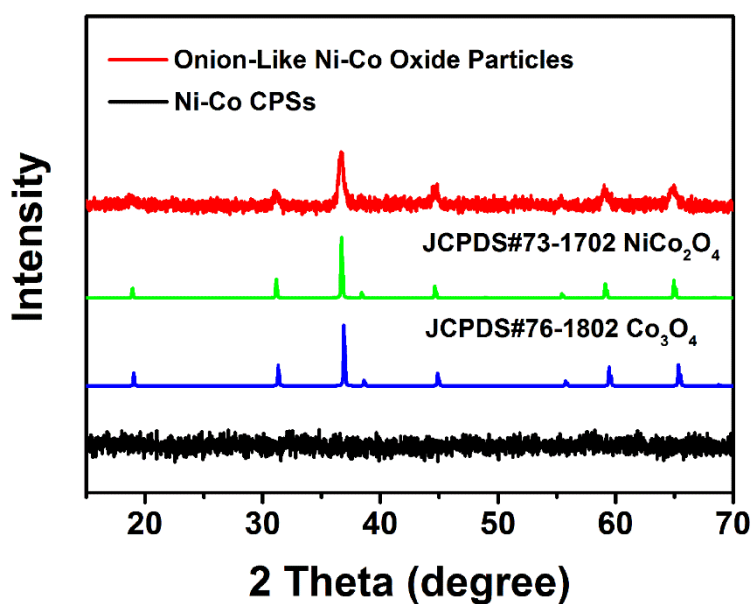

Figure S2. XRD patterns of Ni-Co CPSs and multi-shelled Ni-Co oxide particles and standard patterns of $NiCo_2O_4$ and Co_3O_4.
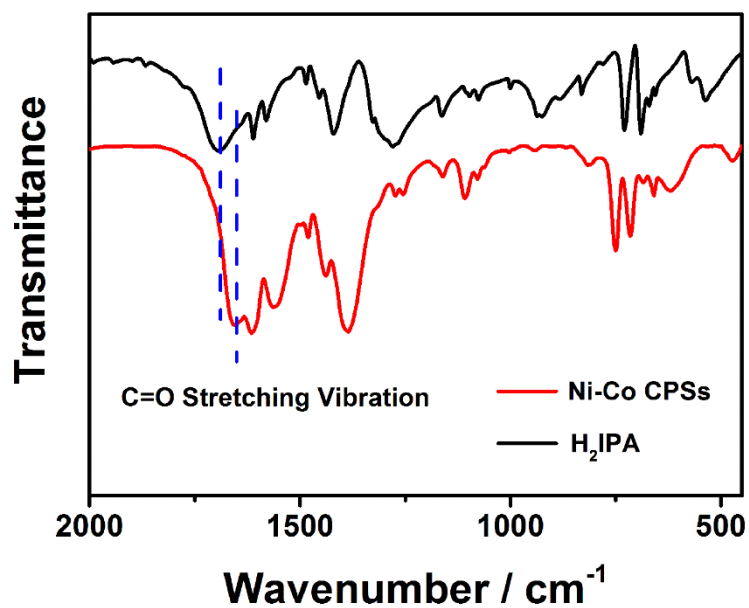
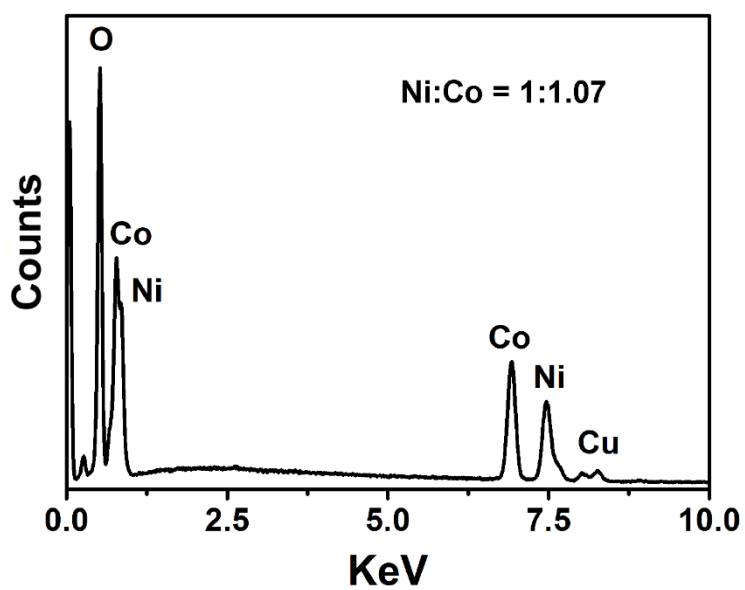**Figure S3.** FTIR spectra of Ni-Co CPSs and isophthalic acid (H_2IPA).

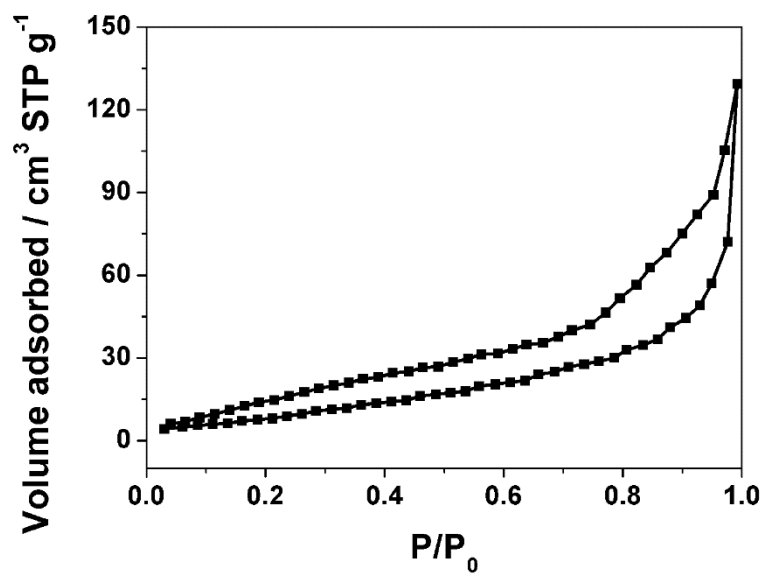**Figure S4.** EDX spectrum for multi-shelled Ni-Co oxide particles.

Figure S5. N_2 adsorption-desorption isotherm of multi-shelled Ni-Co oxide particles. The desorption does not close at the relative pressure of about 0.4 may be due to relatively low mass of the sample.
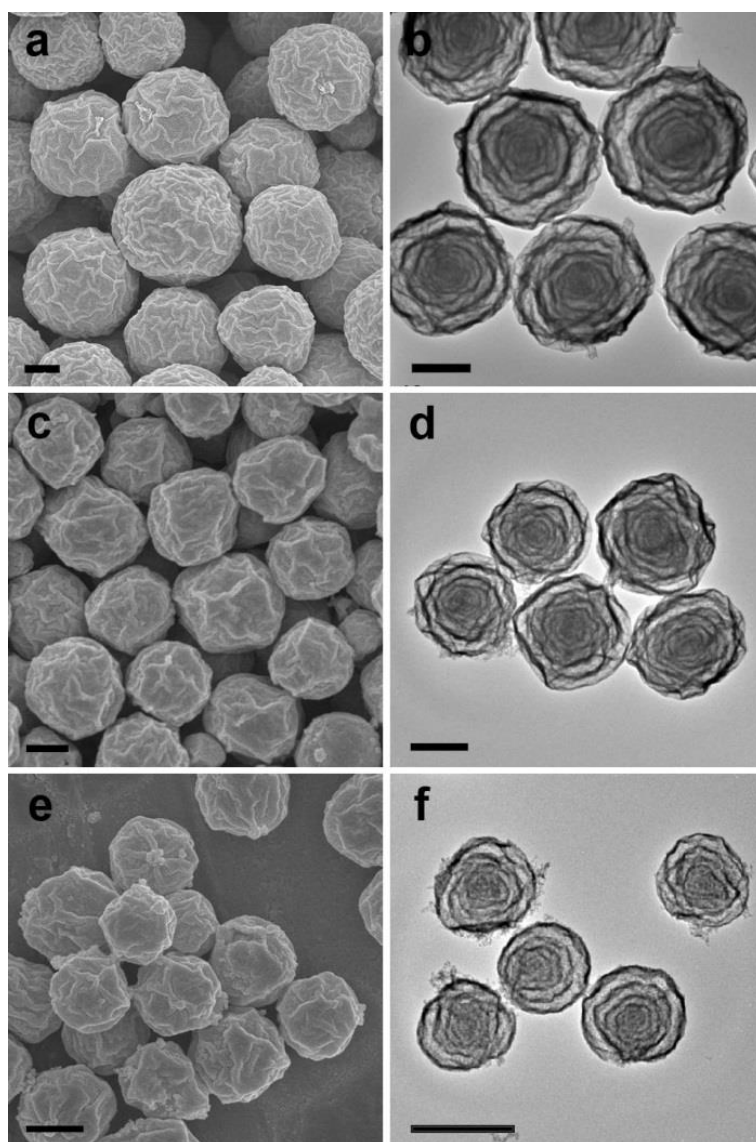
Figure S6. FESEM and TEM images of multi-shelled Ni-Co oxide particles with different sizes: (a, b) 1600 nm, (c, d) 800 nm, and (e, f) 500 nm. The scale bars are 500 nm.
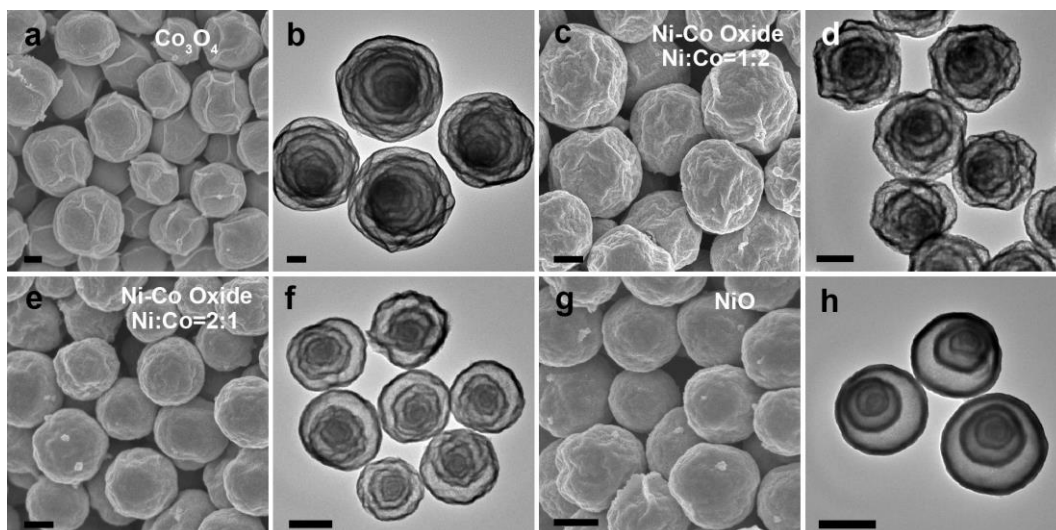
Figure S7. FESEM and TEM images of multi-shelled particles with different molar ratios of Ni and Co elements: (a, b) Co_3O_4, (c, d) Ni-Co oxide with Ni/Co molar ratio of 1:2, (e, f) Ni-Co oxide with Ni/Co molar ratio of 2:1, and (g, h) NiO multi-shelled particles. The scale bars are 500 nm.
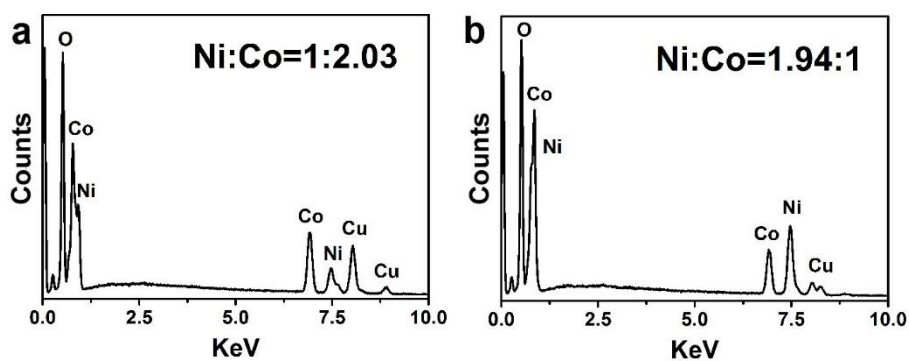

Figure S8. EDX spectra for multi-shelled Ni-Co oxide particles with Ni/Co molar ratios of (a) 1:2 and (b) 2:1.
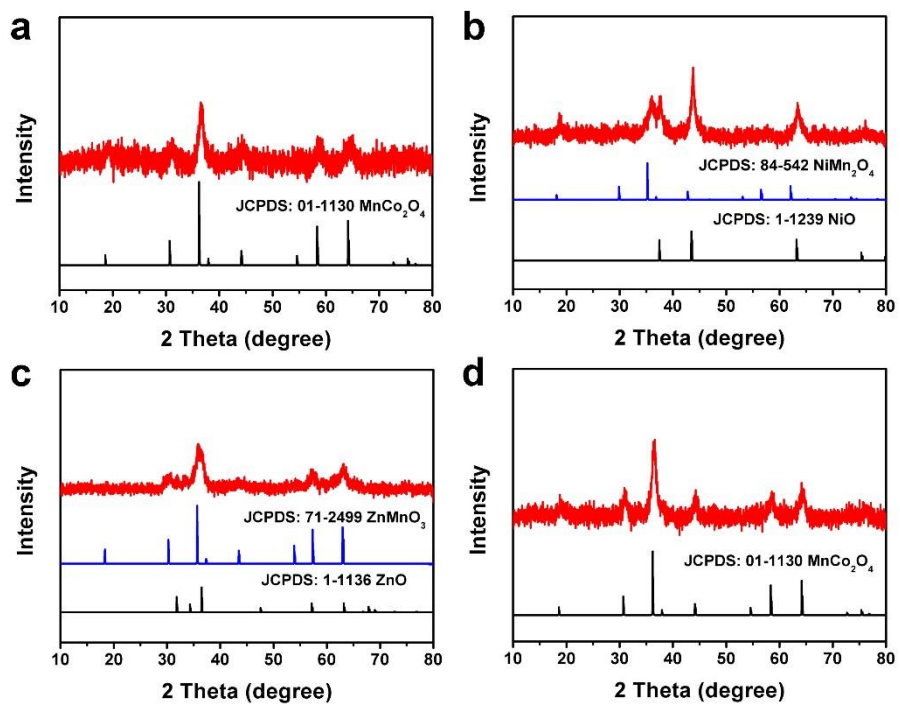
Figure S9. XRD patterns of Mn-Co oxide, Mn-Ni oxide, Zn-Mn oxide, and Mn-Co-Ni oxide multi-shelled particles.
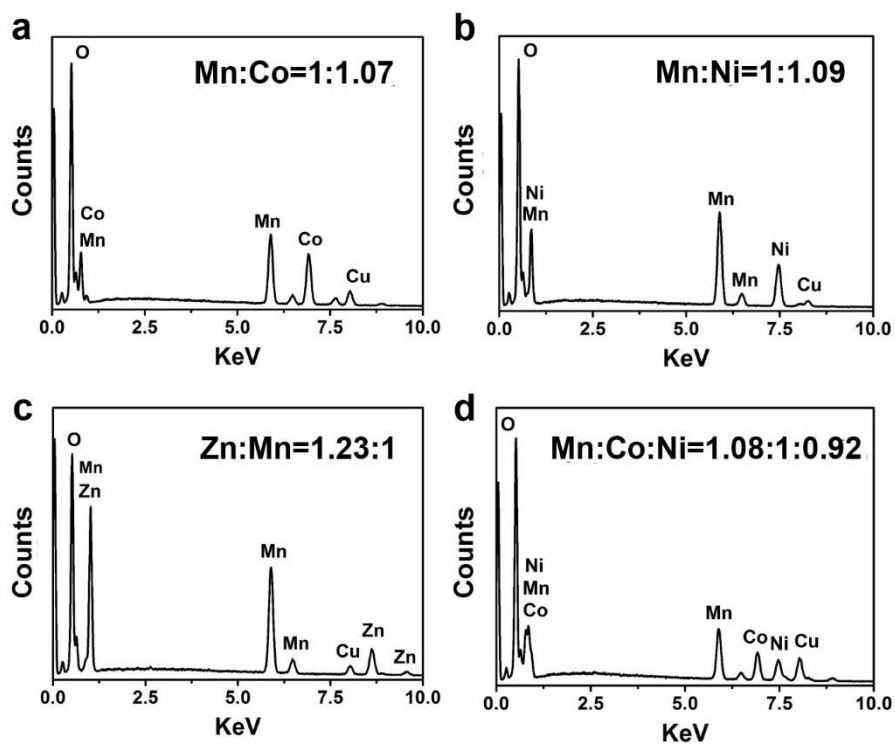
Figure S10. EDX spectra for (a) Mn-Co oxide, (b) Mn-Ni oxide, (c) Zn-Mn oxide, and (d) Mn-Co-Ni oxide multi-shelled particles.
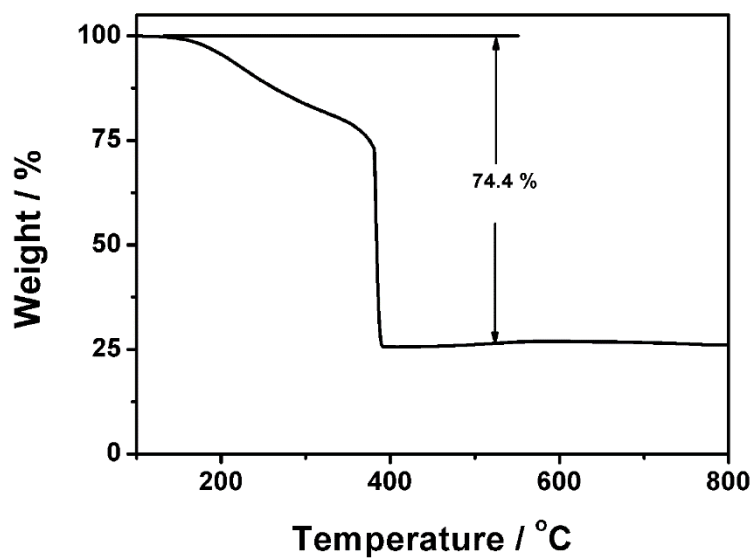

Figure S11. TGA profile for the Ni-Co CPSs.
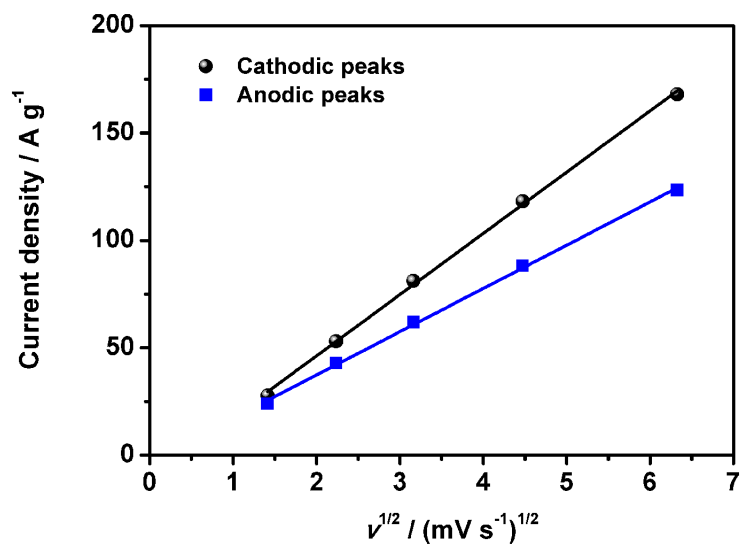
Figure S12. Dependence of the peak current density on square root of sweep rate for the multi-shelled Ni-Co oxide particle electrode.
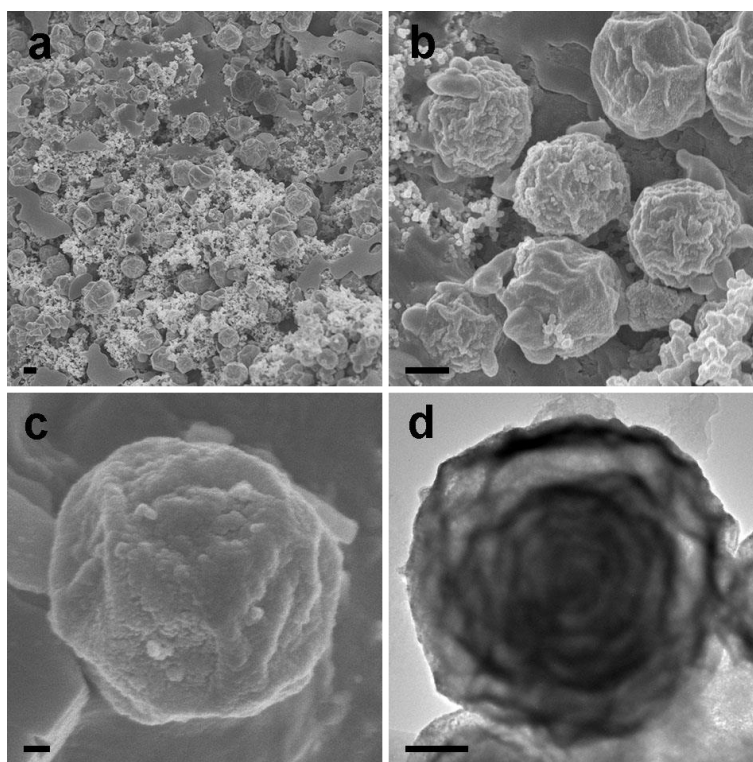
Figure S13. Microscopy characterizations of multi-shelled Ni-Co oxide particles after cycling for 20000 cycles. (a, b, c) FESEM images and (d) TEM image of multi-shelled Ni-Co oxide particles after cycling for 20000 cycles at a current density of 10 A g^{-1}. Scale bars: (a, b) 500 nm, (c) 100 nm, and (d) 200 nm.
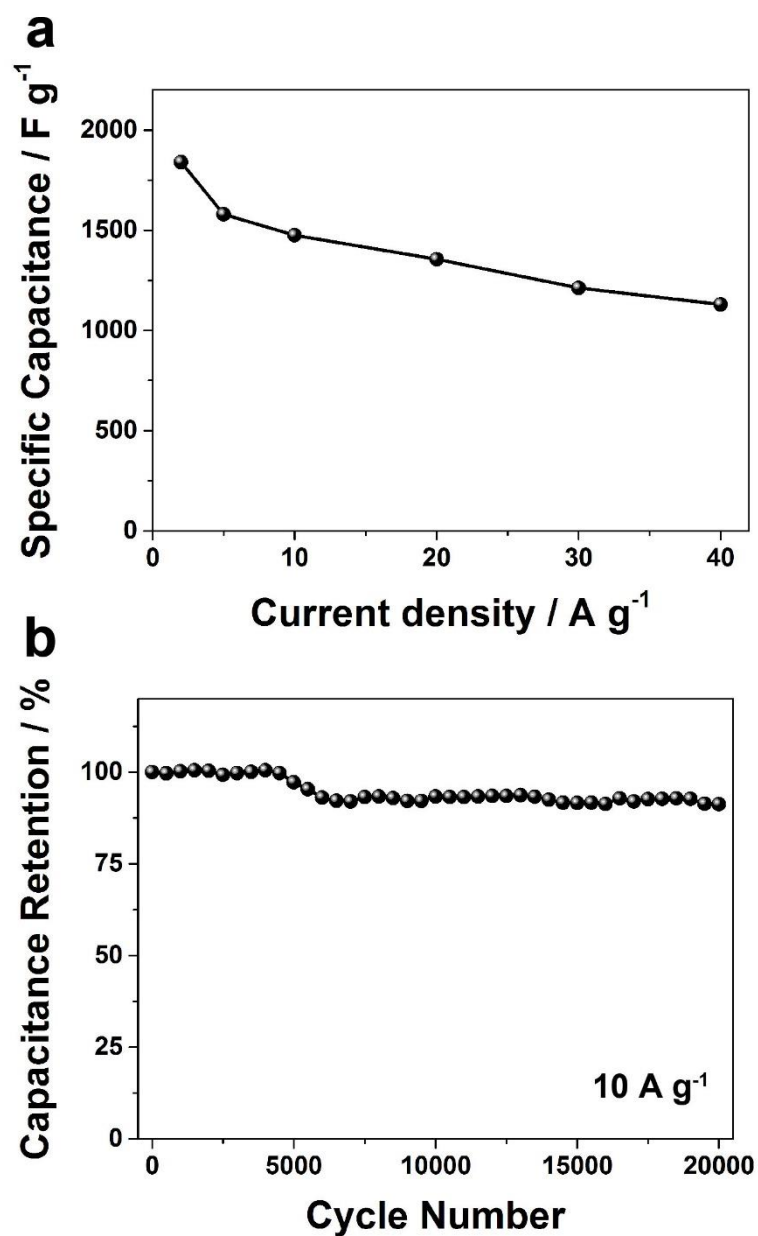
Figure S14. Electrochemical characterizations of the multi-shelled Ni-Co oxide particles with Ni/Co molar ratio of 1:2. (a) Specific capacitance at different discharge current densities and (b) cycling performance at a constant current density of 10 A g^{-1}.

Figure S15. Microscopy characterizations and electrochemical performance of graphene/multi-shelled mesoporous carbon sphere (G/MMCS) composites. (a) FESEM image and (b) TEM image of G/MMCS composites. The scale bars are 200 nm. (c) Cyclic voltammetry (CV) curve at 5 mV s^{-1}. (d) Galvanostatic charge-discharge voltage profiles at a current density of 1 A g^{-1}.

Table S1. Electrochemical performance of different Ni-Co oxide, Ni-Co oxide composite and other mixed metal oxide based electrodes.

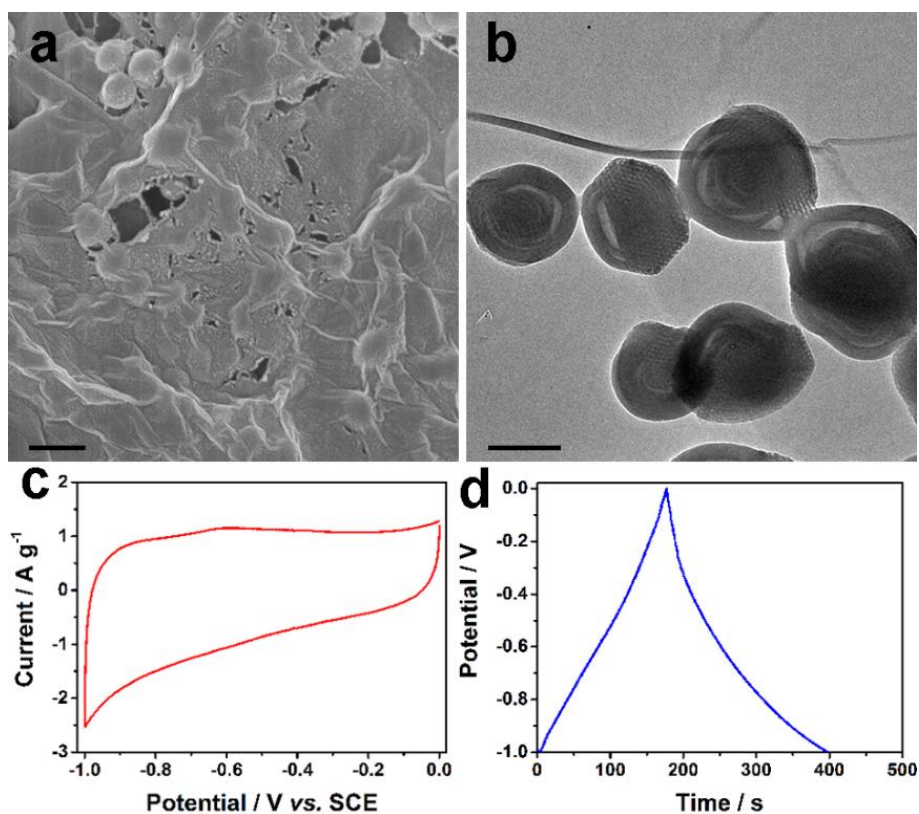| Reference	Type of materials	Capacitance retention after cycling	Specific capacitance (F g^{-1})	Rate performance
This work	Multi-shelled Ni-Co oxide particles	93.5% (20000 cycles)	1907 (2 A g^{-1})	72% from 2 to 20 A g^{-1}
4	$NiCo_2O_4$ tube-in-tube structures	Not reported	1756 (1 A g^{-1})	83% from 2 to 20 A g^{-1}
5	$NiCo_2O_4$ nanowires	91.4% (2000 cycles)	1197 (1 A g^{-1})	52% from 1 to 8 A g^{-1}
6	$NiCo_2O_4$ core-double-shell spheres	94.7% (4000 cycles)	1141 (1 A g^{-1})	69% from 1 to 15 A g^{-1}
7	$NiCo_2O_4$ nanowires	80% (3000 cycles)	722 (1 A g^{-1})	79% from 1 to 20 A g^{-1}
8	$NiCo_2O_4$ nanotubes	93.6% (3000 cycles)	1647 (1 A g^{-1})	77% from 1 to 25 A g^{-1}
9	$NiCo_2O_4$ spheres	93.2% (1000 cycles)	1006 (1 A g^{-1})	72% from 1 to 20 A g^{-1}
10	$NiCo_2O_4$ nanowires	93.8% (3000 cycles)	743 (1 A g^{-1})	79% from 1 to 40 A g^{-1}
11	Mesoporous $NiCo_2O_4$ nanowires	90% (5000 cycles)	401 (1 A g^{-1})	75% from 1 to 8 A g^{-1}
12	Urchin-like $NiCo_2O_4$ spheres	90.8% (2000 cycles)	1650 (1 A g^{-1})	82% from 1 to 15 A g^{-1}
13	Hierarchical mesoporous $NiCo_2O_4$ spheres	~100% (1000 cycles)	1619 (2 A g^{-1})	35% from 2 to 10 A g^{-1}
14	$NiCo_2O_4$ microspheres	97.5% (3000 cycles)	1284 (2 A g^{-1})	77% from 2 to 20 A g^{-1}
15	Mesoporous hollow $NiCo_2O_4$ spheres	87% (3200 cycles)	678 (1 A g^{-1})	80% from 1 to 10 A g^{-1}

16	$NiCo_2O_4$ aerogel	91% (2000 cycles)	1400 (25 mV s^{-1})	Not reported
17	$NiCo_2O_4$/Co_3O_4 double-shelled nanocages	92.5% (12000 cycles)	972 (5 A g^{-1})	63% from 5 to 50 A g^{-1}
18	$NiCo_2O_4$/carbon aerogels	97.6% (2000 cycles)	1700 (25 mV s^{-1})	50% from 25 to 500 mV s^{-1}
19	$NiCo_2O_4$/CNF nanocomposites	92.7% (2400 cycles)	1002 (1 A g^{-1})	52% from 1 to 20 A g^{-1}
20	$NiCo_2O_4$/CNT nanocomposites	94.1% (2000 cycles)	1642 (0.5 A g^{-1})	54% from 0.5 to 20 A g^{-1}
21	$NiCo_2O_4$/GO nanocomposites	90.8% (2000 cycles)	1693 (1 A g^{-1})	68% from 1 to 16 A g^{-1}
22	NiO/$NiCo_2O_4$/ Co_3O_4 composites	94.9% (1000 cycles)	1717 (0.625 A g^{-1})	71% from 0.625 to 6.25 A g^{-1}
23	$NiCo_2O_4$ nanosheets/ halloysite nanotubes	94.7% (10000 cycles)	1887 (6 A g^{-1})	79% from 6 to 30 A g^{-1}
24	$NiCo_2O_4$ hexagonal ring/graphene hybrid	93% (5000 cycles)	1337 (1 A g^{-1})	78% from 1 to 12 A g^{-1}
25	Mesoporous $MnCo_2O_4$ nanoflake	93.3% (2000 cycles)	1487 (1 A g^{-1})	64% from 1 to 10 A g^{-1}
26	Chain-like $NiWO_4$ nanoparticles	90% (1000 cycles)	173 (5 mV s^{-1})	Not reported
27	$CoMoO_4$-$NiMoO_4$ nanocomposites	75.1% (1000 cycles)	1039 (0.625 A g^{-1})	72% from 0.625 to 25 A g^{-1}
28	$NiMoO_4$/ graphene nanocomposites	88% (1000 cycles)	367 (5 A g^{-1})	79% from 5 to 20 A g^{-1}
29	$MnMoO_4$/ $CoMoO_4$ nanowires	98% (1000 cycles)	187 (1 A g^{-1})	66% from 0.5 to 3 A g^{-1}

Table S2. Energy and power densities of different Ni-Co oxide based electrodes.

Reference	Type of materials	Energy density (Wh kg^{-1})	Power density (W kg^{-1})
4	$NiCo_2O_4$ tube-in-tube structures	59.7	800
30	Flower-like Ni-Co oxide	34.9	875
31	$NiCo_2O_4$ nanoneedle array/carbon aerogel hybrid	47.5	400
32	$NiCo_2O_4$ nanosheets on carbon cloth	60.9	568.2
33	Dandelion-like $NiCo_2O_4$ microspheres/ nanomeshes	45.3	533.3
34	Network-like mesoporous $NiCo_2O_4$ on carbon cloth	38.3	396
35	Carbon foam/$NiCo_2O_4$	47.8	640
36	Porous $NiCo_2O_4$ spheres	27.8	128
37	$NiCo_2O_4$ nanotubes	19.6	782.6
38	3D Ni-Co oxide	36.5	142
This work	Multi-shelled Ni-Co oxide particles	52.6	1604

Supporting References

[1]   J. Liu, T. Yang, D.-W. Wang, G. Q. Lu, D. Zhao, S. Z. Qiao, *Nat. Commun.* **2013**, *4*, 2798.

[2]   L. Shen, L. Yu, H. B. Wu, X.-Y. Yu, X. Zhang, X. W. Lou, *Nat. Commun.* **2015**, *6*, 6694.

[3]   A. Kushima, T. Koido, Y. Fujiwara, N. Kuriyama, N. Kusumi, J. Li, *Nano Lett.* **2015**, *15*, 8260.

[4]   S. Peng, L. Li, Y. Hu, M. Srinivasan, F. Cheng, J. Chen, S. Ramakrishna, *ACS Nano* **2015**, *9*, 1945.

[5]   C. An, Y. Wang, Y. Huang, Y. Xu, L. Jiao, H. Yuan, *Nano Energy* **2014**, *10*, 125.

[6]   L. Shen, L. Yu, X.-Y. Yu, X. Zhang, X. W. Lou, *Angew. Chem. Int. Ed.* **2015**, *54*, 1868.

[7]   H. Wang, Q. Gao, L. Jiang, *Small* **2011**, *7*, 2454.

[8]   L. Hu, Y. Huang, F. Zhang, Q. Chen, *Nanoscale* **2013**, *5*, 4186.

[9]   Y. Lei, J. Li, Y. Wang, L. Gu, Y. Chang, H. Yuan, D. Xiao, *ACS Appl. Mater. Interfaces* **2014**, *6*, 1773.

[10]   H. Jiang, J. Ma, C. Li, *Chem. Commun.* **2012**, *48*, 4465.

[11]   C. Yuan, J. Li, L. Hou, L. Yang, L. Shen, X. Zhang, *J. Mater. Chem.* **2012**, *22*, 16084.

[12]   Q. Wang, B. Liu, X. Wang, S. Ran, L. Wang, D. Chen, G. Shen, *J. Mater. Chem.* **2012**, *22*, 21647.

[13]   Y. Zhang, M. Ma, J. Yang, H. Su, W. Huang, X. Dong, *Nanoscale* **2014**, *6*, 4303.

[14]   R. Zou, K. Xu, T. Wang, G. He, Q. Liu, X. Liu, Z. Zhang, J. Hu, *J. Mater. Chem. A* **2013**, *1*, 8560.

[15]   C. Yuan, J. Li, L. Hou, J. Lin, G. Pang, L. Zhang, L. Lian, X. Zhang, *RSC Adv.* **2013**, *3*, 18573.

[16]   T.-Y. Wei, C.-H. Chen, H.-C. Chien, S.-Y. Lu, C.-C. Hu, *Adv. Mater.* **2010**, *22*, 347.

[17]   H. Hu, B. Guan, B. Xia, X. W. Lou, *J. Am. Chem. Soc.* **2015**, *137*, 5590.

[18]   H.-C. Chien, W.-Y. Cheng, Y.-H. Wang, S.-Y. Lu, *Adv. Funct. Mater.* **2012**, *22*, 5038.

[19]   G. Zhang, X. W. Lou, *Sci. Rep.* **2013**, *3*, 1470.

[20]   X. Wang, X. Han, M. Lim, N. Singh, C. L. Gan, M. Jan, P. S. Lee, *J, Phys. Chem. C* **2012**, *116*, 12448.

[21]   L. Wang, X. Wang, X. Xiao, F. Xu, Y. Sun, Z. Li, *Electrochim. Acta* **2013**, *111*, 937.

[22]   M.-C. Liu, L.-B. Kong, C. Lu, X.-M. Li, Y.-C. Luo, L. Kang, *ACS Appl. Mater. Interfaces* **2012**, *4*, 4631.

[23]   J. Liang, Z. Fan, S. Chen, S. Ding, G. Yang, *Chem. Mater.* **2014**, *26*, 4354.

[24]   C. Nethravathi, C. R. Rajamathi, M. Rajamathi, X. Wang, U. K. Gautam, D. Golberg, Y. Bando, *ACS Nano* **2014**, *8*, 2755.

[25]   A. K. Mondal, D. Su, S. Chen, A. Ung, H.-S. Kim, G. Wang, *Chem. Eur. J.* **2015**, *21*, 1526.

[26]   U. Nithiyanantham, S. R. Ede, S. Anantharaj, S. Kundu, *Cryst. Growth Des.* **2015**, *15*, 673.

[27]   M.-C. Liu, L.-B. Kong, C. Lu, X.-J. Ma, X.-M. Li, Y.-C. Luo, L. Kang, *J. Mater. Chem. A* **2013**, *1*, 1380.

[28]   D. Ghosh, S. Giri, C. K. Das, *Nanoscale* **2013**, *5*, 10428.

[29]   L.-Q. Mai, F. Yang, Y.-L. Zhao, X. Xu, L. Xu, Y.-Z. Luo, *Nat. Commun.* **2011**, *2*, 381.

[30]   J. Zhang, F. Liu, J. P. Cheng, X. B. Zhang, *ACS Appl. Mater. Interfaces* **2015**, *7*, 17630.

[31]   P. Hao, J. Tian, Y. Sang, C.-C. Tuan, G. Cui, X. Shi, C. P. Wong, B. Tang, H. Liu, *Nanoscale* **2016**, *8*, 16292.

[32]   Z. Gao, W. Yang, J. Wang, N. Song, X. Li, *Nano Energy* **2015**, *13*, 306.

[33]   L. Liu, H. Zhang, J. Yang, Y. Mu, Y. Wang, *J. Mater. Chem. A* **2015**, *3*, 22393.

[34]   S. Gao, F. Liao, S. Ma, L. Zhu, M. Shao, *J. Mater. Chem. A* **2015**, *3*, 16520.

[35]   J. Wang, L. Shen, P. Nie, X. Yun, Y. Xu, H. Dou, X. Zhang, *J. Mater. Chem. A* **2015**, *3*, 2853.

[36]   Y. Zhu, Z. Wu, M. Jing, H. Hou, Y. Yang, Y. Zhang, X. Yang, W. Song, X. Jia, X. Ji, *J. Mater. Chem. A* **2015**, *3*, 866.

[37]   J. Zhu, Z. Xu, B. Lu, *Nano Energy* **2014**, *7*, 114.

[38]   Y.-M. Wang, X. Zhang, C.-Y. Guo, Y.-Q. Zhao, C.-L. Xu, H.-L. Li, *J. Mater. Chem. A* **2013**, *1*, 13290.